

# Open Research Online

---

The Open University's repository of research publications and other research outputs

## Effect of pre-emptive in situ parameter modification on residual stress distributions within selective laser-melted Ti6Al4V components

### Journal Item

#### How to cite:

Ali, Haider; Ghadbeigi, Hassan; Hosseinzadeh, Foroogh; de Oliveira, Jeferson and Mumtaz, Kamran (2019). Effect of pre-emptive in situ parameter modification on residual stress distributions within selective laser-melted Ti6Al4V components. The International Journal of Advanced Manufacturing Technology, 103(9-12) pp. 4467–4479.

For guidance on citations see [FAQs](#).

© 2019 The Authors



<https://creativecommons.org/licenses/by/4.0/>

Version: Version of Record

Link(s) to article on publisher's website:

<http://dx.doi.org/doi:10.1007/s00170-019-03860-6>

---

Copyright and Moral Rights for the articles on this site are retained by the individual authors and/or other copyright owners. For more information on Open Research Online's data [policy](#) on reuse of materials please consult the policies page.

---

[oro.open.ac.uk](http://oro.open.ac.uk)



# Effect of pre-emptive in situ parameter modification on residual stress distributions within selective laser-melted Ti6Al4V components

Haider Ali<sup>1</sup> · Hassan Ghadbeigi<sup>1</sup> · Foroogh Hosseinzadeh<sup>2</sup> · Jeferson Oliveira<sup>2</sup> · Kamran Mumtaz<sup>1</sup> 

Received: 13 February 2019 / Accepted: 7 May 2019  
© The Author(s) 2019

## Abstract

The effect of thermally induced residual stresses is not dynamically considered during a selective laser melting (SLM) build; instead, it processes using invariable parameters across the entire component's cross-section. This lack of pre-emptive in situ parameter adjustment to reduce residual stresses during processing is a lost opportunity for the process with the potential to improve component mechanical properties. This investigation studied the residual stresses introduced during manufacturing of SLM Ti6Al4V benchmark components and adapted process parameters within a build (layer-to-layer specific modifications) to manage and redistribute stresses within these components. It was found that temporarily switching to an increased layer thickness during the build, directly below highly stressed regions within the component, redistributed stresses and reduced the overall stresses within the structure by 8.5% (within the 80–320-MPa residual stress range) compared to standard invariable SLM processing parameters. This work demonstrates the need for current SLM systems to focus on developing a more intelligent processing architecture with parameters that adapt on the fly during a build, in order to manage residual stresses within the built structure.

**Keywords** Residual stress · Geometrical dependence · Cooling rate · Selective laser melting · Additive manufacturing · Ti6Al4V · Contour method

## 1 Introduction

Additive manufacturing (AM) techniques are gradually being adopted by high value, high-performance industries (i.e. aerospace, automotive) due to the greatly expanded design freedoms and parts customization [1–3]. Selective laser melting (SLM) is an AM technique that creates high-density 3D parts by selectively melting and fusing metallic powder. Cross-sections of a 3D geometry are successively fused on top of each other in a layer-wise manner. A significant challenge associated with the manufacture of SLM metallic components is the potential development of high internal residual stress [3]. Rapid repeated heating and cooling cycles of successive layers of the powder feed-

stock during the SLM build process results in high cooling rates and large temperature gradients associated with the process generating high residual stress build up in the SLM built components. Parts can fail during an SLM build, or later in service, due to these high internal residual stresses [3–12]. Post-processing stress relief heat treatment cycles can potentially remove most of the internal residual stresses, but adds up to the manufacturing time and cost of SLM components [13].

A correct understanding of the numerous physical phenomena associated with this complex fabrication process is required in order to prevent defects from forming [14]. All additive manufacturing processes including SLM can be broken down into pre-process, in-process and post-process stages with varying parameters at each stage affecting the final part properties [2, 12]. Considerable research has focused on the in-process parameters and their effect on the residual stress build up in the SLM components; within this work, there is some consensus but also some contradiction, primarily due to the variation in benchmark components tested during these studies [3, 5, 6, 8, 9, 11, 15–27].

✉ Kamran Mumtaz  
K.mumtaz@sheffield.ac.uk

<sup>1</sup> Department of Mechanical Engineering, University of Sheffield, Sheffield, UK

<sup>2</sup> School of Engineering & Innovation, The Open University, Milton Keynes MK7 6BJ, UK

## 1.1 SLM residual stress reduction

The SLM process can be approximated by stacking of thousands of welds together. Understanding the dynamics of a single weld or in SLM terminology, a single melt pool is important. Melt pool size increases with increasing energy input [28]. Laser power has a more pronounced effect on maximum temperature than laser exposure time [28]. Lower laser power leads to lower maximum temperature [28–30], smaller melt pool and higher cooling rates [29]. High laser power results in lower deformation and lower residual stress [25], while Alimardani et al. [30] reported lower residual stresses for lower laser power. Lower scan speed leads to lower temperature gradients [21], lower cooling rates [29], lower residual stresses [31] and reduces the potential for geometric deformation. Higher scan speed leads to increased cooling rate and increased cracking [32], while Pohl et al. [24] reported lower deformation for higher scan speed. Lower power and higher exposure combination (for constant energy density) lead to increased porosity and thus reduced yield strength in 316-L SLM samples [33]. Ali et al. [34] reported lower residual stress for lower power and higher exposure combination (for constant energy density). According to Ali et al. [34] for an energy density of  $76.92 \frac{\text{J}}{\text{mm}^2}$ , SLM Ti6Al4V blocks manufactured with 150 W power and 133- $\mu\text{s}$  exposure combination resulted in 34.6% lower residual stress compared to their 200 W power and 100- $\mu\text{s}$  exposure counterparts [34].

### 1.1.1 Effect of layer thickness

Powder particle size determines the lower limit of the layer thickness, while the need for melt pool penetration into underlying layers determines the upper limit. Larger layer thicknesses can increase productivity at the detriment of geometrical resolution and as well as the roughness of side surfaces. It has been reported [5, 8, 9] that increasing layer thickness results in reduced residual stresses due to a reduction in cooling rate. Kruth et al. [5] reported that for the same energy density, doubling the layer thickness reduced the curling angle of bridge geometry by 6%. Roberts et al. [11] found that doubling the layer thickness reduced the residual stress by 5%. While Zaeh et al. [8] reported that increasing the layer thickness by 2.5 times decreased the deformation of the ends of a T-shaped cantilever by 82%. Sufiiarov et al. [35] reported an increase in yield strength and a decrease in elongation for decreasing layer thickness in IN718 SLM parts. Guan et al. [36] reported that layer thickness had no effect on the mechanical properties of 304 stainless steel SLM components. Delgado et al. [37] reported that increasing layer thickness had a negative effect on the mechanical properties of AISI 316-L SLM components. Parts are created with different layer

thickness using the same parameters [5, 8, 9, 11, 35–37], optimised for one layer thickness (i.e. achieving full density). The work by Ali et al. [34] optimised parameters for each layer thickness and found that 75- $\mu\text{m}$  layer thickness blocks had 27.1% less residual stress compared to their 50- $\mu\text{m}$  layer thickness counterparts [34].

### 1.1.2 Effect of geometry

SLM part length and moment of inertia of the build section affects the magnitude of the residual stress build up [27]. According to Casavola et al. [3], circular specimens warp (due to residual stress) less as opposed to components where the geometrical dimensions have a higher aspect ratio. This work also concluded that for the same diameter, thicker specimens have lower stresses as opposed to thinner specimens. Yadroitsava et al. [22] compared residual stresses in a parallelepiped built directly onto the substrate with a cantilever beam, where the overhanging parts were supported and found that the residual stresses in the cantilever structure were much higher than the parallelepiped. This work concluded that residual stress depends on the material properties, as well as sample and supports geometry. Mugwagwa et al. [38] studied the effect of geometrical features on residual stress using a T-shaped geometry and concluded that higher residual stresses are generated at sharper edges of the specimens and increasing the curvature of the corners relaxed these stresses due to a reduction in sharpness.

Ali et al. [34, 39–42] measured residual stress with the strain gage hole-drilling method [34, 39–45] in SLM Ti6Al4V  $30 \times 30 \times 10$  mm blocks. Residual stress is inversely proportional to bed temperature and 570 °C bed pre-heat temperature completely mitigated residual stress [42]. Residual stress is inversely proportional to layer thickness and 75- $\mu\text{m}$  layer thickness resulted in minimum residual stress [40]. For constant energy density of  $76.9 \frac{\text{J}}{\text{mm}^2}$ , 150 W power and 133- $\mu\text{s}$  exposure combination resulted in the lowest residual stress [40].

## 1.2 In situ parameter modification for stress reduction/redistribution

Current SLM systems anticipate geometric features (i.e. outer skin, overhanging geometries), support structures and make processing parameter adjustments in order to best fabricate the component. However, the anticipation of internal residual stresses is not accounted for during part fabrication. The SLM process uses the same process parameters for areas within a component that have a very low or very high-stress concentration; this lack of anticipation and in situ adjustment is a lost opportunity that would allow the process to be greatly improved. There is currently no study on the strategic

location-specific application of stress reduction strategies across regions of an SLM component cross-section and its effect on residual stress distribution. This work studies the effect of varying parameters across the building height and applying stress reduction strategies to specific regions across the cross-section of SLM Ti6Al4V components. Specifically, the effect of varying laser power and exposure combinations for a constant energy density and layer thickness on residual stress on an SLM Ti6Al4V I-Beam section is undertaken. The contour method is used for residual stress measurement and Matlab image analysis is used in combination with experimental trials to understand the underlying phenomena associated with the residual stress build up in a complex SLM Ti6Al4V sample.

## 2 Experimental methodology

### 2.1 Material and processing parameters

Table 1 shows the composition of Ti6Al4V-ELI powder with a particle size of 15–45  $\mu\text{m}$  from Technik Spezialpulver (TLS), used within this investigation.

Both SLM125 [42] and AM250 [39] have a maximum power of 200 W. Previous work from both systems for parameter optimisation trials showed that 200 W power and 100- $\mu\text{s}$  exposure combination led to nearly fully dense (99.9%) parts for 100 °C bed temperatures [39, 42]. Therefore, the manufacturing of benchmark test specimens was carried out on a standard Renishaw AM250 machine using the process parameters presented in Table 2. A high bed temperature sample was manufactured using a modified Renishaw SLM125 machine with retrofitted high-temperature platform at the University of Sheffield.

### 2.2 Density and microstructure analysis

Density and microstructure for parameter combinations shown in Table 3 were analysed based on an optical microscopy methodology presented in the work by Ali et al. [39, 42].

### 2.3 Application of location-specific residual stress reduction strategies

Experiments were designed to first establish a benchmark for residual stress concentration studies in an I-Beam geometry. SLM stress reduction strategies (developed based on  $30 \times$

$30 \times 10$  mm block samples and strain gage hole-drilling method) identified in the work by Ali et al. [34] were then applied locally to these identified high-stress areas to understand their local effect in an I-Beam geometry. I-Beam sections were designed (see Fig. 1a) and built on the SLM250 platform using optimum SLM parameters for Ti6Al4V, found in the work by Ali et al. [34]. The contour method was used to measure residual stress in the I-Beam, cross-sectioned through the XZ plane. The 2D residual stress map identified the high-stress regions in the I-Beam. Figure 1b shows the dimensions of the four regions for strategic application of residual stress reduction strategies, across the height of the entire cross-section. Table 4 shows the details of the different I-Beam test cases manufactured for this study.

In test case IB-1, the standard I-Beam was manufactured using the optimum combination of parameters for 50- $\mu\text{m}$  layer thickness to obtain the highest density as is reported in [34, 42]. The work by Ali et al. [34] showed that increasing layer thickness reduces residual stress. From the different layer thicknesses evaluated in the work (25, 50 and 75  $\mu\text{m}$ ), 75- $\mu\text{m}$  layer thickness resulted in the overall lowest stress. Therefore, 75- $\mu\text{m}$  layer thickness was applied as a stress reduction strategy to strategic regions (as shown in Fig. 1b) of test cases IB-2 and IB-5, while the remaining sections were built with an optimum combination of parameters for 50- $\mu\text{m}$  layer thickness from density optimisation trials presented in the work by Ali et al. [34, 42]. It is also reported that [34] for a constant energy density, decreasing power and increasing exposure led to a reduction in residual stress. From the different combinations of power and exposure for a constant energy density of  $76.92 \frac{\text{J}}{\text{mm}^3}$ , was calculated from the optimum combination of parameters for 50- $\mu\text{m}$  layer thickness from density optimisation trials presented in the work by Ali et al. [34, 42] using Eq. 1, 150 W power and 133- $\mu\text{s}$  exposure led to the lowest residual stress in SLM Ti6Al4V parts [34]. Therefore, 150 W power and 133- $\mu\text{s}$  exposure were applied as a stress reduction strategy to strategic regions of test cases IB-3 and IB-6, while the remaining sections were built with optimum combination of parameters (200 W power and 100- $\mu\text{s}$  exposure) for 50- $\mu\text{m}$  layer thickness from density optimisation trials presented in the work by Ali et al. [34, 42].

$$\text{ED} = \frac{P \cdot t}{\text{pd} \cdot h \cdot \text{lt}} \quad (1)$$

where ( $P$ ) stands for power, ( $t$ ) for exposure time, ( $\text{pd}$ ) for point distance, ( $h$ ) for hatch distance, and ( $\text{lt}$ ) for layer thickness. Increasing bed pre-heat temperature led to a reduction in residual stress [34, 42]. Therefore, a bed pre-heat temperature of 570 °C in combination with optimum combination of parameters for 50- $\mu\text{m}$  layer thickness (from density optimisation trials presented in the work by Ali et al. [34, 42]) resulted in a significant reduction in residual stress in SLM Ti6Al4V parts

**Table 1** Chemical composition of Ti6Al4V-ELI powder

Element	N	C	H	Fe	O	Al	V	Ti
% composition	0.006	0.009	0.001	0.2	0.09	6.21	4.08	89.404

**Table 2** SLM benchmark process parameters

Focus offset	Hatch spacing ( $\mu\text{m}$ )	Contour spacing (mm)	Point distance ( $\mu\text{m}$ )	Scanning strategy
0	80	0.2	65	90° alternate

[34, 42]. Therefore, test case IB-4 was built at 570 °C using the optimum combination of parameters (200 W power and 100- $\mu\text{s}$  exposure [34, 42].

Figure 2a shows a representative I-Beam geometry with supports and attached with the substrate. Figure 2b shows an I-Beam geometry cutoff from the substrate and supports removed.

## 2.4 Residual stress maps using the contour method

The contour method is a powerful technique for measuring residual stress in structures that offers some advantages compared with neutron diffraction and deep-hole drilling techniques [46–48]. Namely, it provides a two-dimensional map of residual stress on a cut surface; it can be implemented in the laboratory with widely available cutting and measurement equipment and it is not limited by the microstructure or the thickness of the component. Conceptually, the contour method is simple and involves cutting the sample along a flat plane where residual stresses normal to the cut plane are to be determined. Creation of a free surface completely relieves the residual stress acting normal to the surface and this results in deformation of that surface. The topography of the newly created surfaces is measured and input with opposite sign as a boundary condition in an elastic finite element (FE) model to determine the cross-sectional distribution of undisturbed residual stresses prior to the cut [46–48]. The main steps of the contour method are specimen cutting, surface contour measurement, data analysis and FE modelling.

The contour method has been applied to measure residual stress introduced by various manufacturing processes [49, 50], including welding [51–55], laser-engineered net shaped [56] and SLM [57] components.

The samples were sectioned with an Agie Charmilles EDM machine with a 0.15-mm wire diameter. In order to prevent the introduction of EDM cutting artefacts close to the sample surfaces, sacrificial layers were bonded on to the surfaces of the samples [48]. The samples were figure clamped to the EDM bed table. Cutting was initiated after the specimens

and fixtures had reached thermal equilibrium within the wire EDM deionised water tank.

Likewise, the cut parts were left in the temperature-controlled CMM laboratory prior to starting surface profile measurements to allow them to reach thermal equilibrium with the laboratory environment. The topography of each cut surface was measured on a 0.025-mm grid using a Zeiss Eclipse CMM fitted with a Micro-Epsilon triangulating laser probe. The perimeters of the cut surfaces were also measured for use in the data analysis and FE modelling steps by a 2-mm diameter ruby-tipped Renishaw PH10M touch trigger probe.

For each contour cut, data analysis was conducted using the standard approach described in [47, 48]. 3D FE models based on the measured perimeter of the cut parts were built using the ABAQUS code. Linear hexahedral elements with reduced integration (C3D8R) were used to mesh the models. The material was assumed to have isotropic elastic properties. Displacements derived from the processed measured surface data were applied at the FE nodes of the modelled cut surface, with the reverse sign, as boundary conditions. Three additional restraints were imposed on each FE model to avoid rigid body motion. Linear elastic stress analysis for each case was performed to calculate the residual stresses acting normal to the cut face.

## 3 Results and discussion

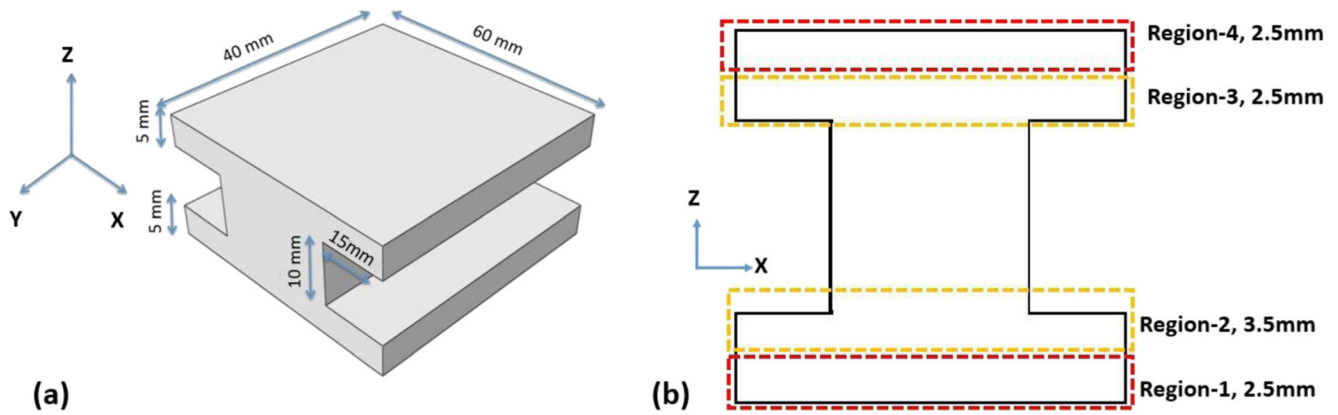
### 3.1 Density and microstructure

Figure 3 depicts density analysis for the various combination of SLM parameters used in the current work. For  $30 \times 30 \times 10$  mm blocks 200 W power and 50- $\mu\text{s}$  exposure at 100 °C bed temperature results in 99.9% density [42]. Due to inter-layer defects, 75- $\mu\text{m}$  SLM Ti6Al4V blocks were 99.2% dense [40]. For constant energy density of  $76.9 \frac{\text{J}}{\text{mm}^3}$  [40] lower power 150 W and higher exposure 133- $\mu\text{s}$  combination resulted in 99.9% dense parts. Two hundred watts and 100  $\mu\text{s}$  with 570 °C bed temperature resulted in 99.8% dense SLM

**Table 3** SLM processing conditions

Parameters	Power (W)	Layer thickness ( $\mu\text{m}$ )	Exposure ( $\mu\text{s}$ )	Bed temperature (°C)
Standard	200	50	100	100
High layer thickness	200	75	140	100
Low power/high exposure	150	50	133	100
High bed temperature	200	50	100	570





**Fig. 1** **a** Dimensioned I-Beam geometry; **b** I-Beam regions for strategic application of stress reduction strategies

Ti6Al4V parts [42]. This shows that all parameter combinations in this study will result in a density higher than 99%.

Figure 4 shows that irrespective of the used parameter combinations, prior columnar  $\beta$  grains, which are characteristics of SLM build Ti6Al4V parts, exists in all samples. Figure 4a–c shows that the microstructure is martensitic [40, 42]. According to Ahmed et al. [58], cooling rates higher than  $410 \frac{^{\circ}\text{C}}{\text{s}}$  leads to a fully martensitic microstructure for Ti6Al4V. The works by Ali et al. [40–42] show that the cooling rate for all combination of SLM parameters used in this study was higher than  $410 \frac{^{\circ}\text{C}}{\text{s}}$  and therefore lead to martensitic  $\alpha'$  laths formation in the samples as in Fig. 4a–c. Figure 4d shows that at a bed temperature of  $570^{\circ}\text{C}$ , the sample contains a basket weave ( $\alpha + \beta$ ) microstructure with  $\alpha$  colonies (highlighted by red circles). This is due to the fact that the martensitic decomposition of Ti6Al4V is in the range of  $600\text{--}650^{\circ}\text{C}$  [59–61]; however, with a bed temperature of about  $570^{\circ}\text{C}$  and after completion of the build, the cooling rate is only  $30 \frac{^{\circ}\text{C}}{\text{min}}$ , which is much lower than the cooling rate required for martensitic formation in Ti6Al4V [42].

### 3.2 Residual stress profile map for standard processing conditions

Figure 5 shows the map of residual stress distribution for test case IB-1 measured using the contour method. Black dashed rectangles highlight the regions with high residual stress with the maximum residual stress level of 320 MPa. The high-stress region 2, the corners between the lower flange and

bottom section of the web identified in Fig. 5 are aligned with the findings reported in [62] reported indicating high levels of residual stress occur at the boundary between the substrate and DMLS samples. Likewise, the location of another high-stress region was identified as region 4; the top of the I-Beam geometry is aligned with the findings reported by Casavola et al. [3], Furomoto et al. [62] and Van Belle et al. [63] in that the highest residual stress occurring in the top surface of the built component.

### 3.3 Strategic application of residual stress reduction strategies

The work by Ali et al. [34] showed that various processing conditions (i.e. increasing the layer thickness to  $75 \mu\text{m}$ , decreasing the power/increasing exposure time and pre-heating the powder bed) were able to reduce residual stress when uniformly applied across a cube SLM component. These stress reduction strategies were applied to various regions detailed in Fig. 1b and Table 4. The resultant residual stress maps are shown in Fig. 6.

### 3.4 Effect of strategic stress reduction strategies on residual stress

A Matlab image analysis script was developed to extract the area associated with each stress level in regions 1, 2, 3 and 4 for all the test cases shown in Table 4. Figure 7 shows

**Table 4** Strategic stress reduction test cases

Test case	Stress reduction strategy
IB-1	Standard parameters (applied to all regions)
IB-2	$75\text{-}\mu\text{m}$ layer thickness to regions 2 and 4 (standard parameters to regions 1 and 3)
IB-3	150 W power and $133\text{-}\mu\text{s}$ exposure to regions 2 and 4 (standard parameters to regions 1 and 3)
IB-4	$570^{\circ}\text{C}$ bed pre-heating on Renishaw SLM-125 machine (applied to all regions)
IB-5	$75\text{-}\mu\text{m}$ layer thickness for regions 1 and 3 (standard parameters to regions 2 and 4)
IB-6	150 W power and $133\text{-}\mu\text{s}$ exposure for regions 1 and 3 (standard parameters to regions 2 and 4)

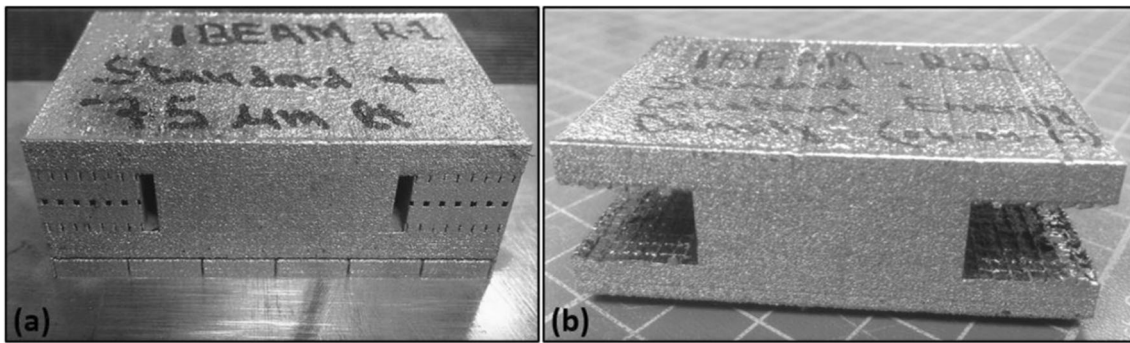


**Fig. 2** **a** I-Beam geometry with supports; **b** I-Beam geometry without supports and removed from substrate plate

corresponding areas (extracted using Matlab Image Processing), with the identified stress levels in region 4 (top of the I-Beam geometry), for all test cases studied shown in Fig. 6.

### 3.4.1 Effect of strategic stress reduction strategies on residual stress in high-stress region 4

The results in Figs. 6b and 8 show that with the application of 75- $\mu\text{m}$  layer thickness to region 4 (identified as the high-stress regions shown in Fig. 5) for test case IB-2 reduced the area corresponding to the maximum residual stress (320 MPa) to 23.5%, with a 7.5% reduction compared with the standard I-Beam (test case IB-1) at similar stress level. Figures 6b and 8 show that, test case IB-2, 160-MPa residual stress region area increased by 29.2% and the 80-MPa residual stress region area decreased by 67.5% compared with test case IB-1.

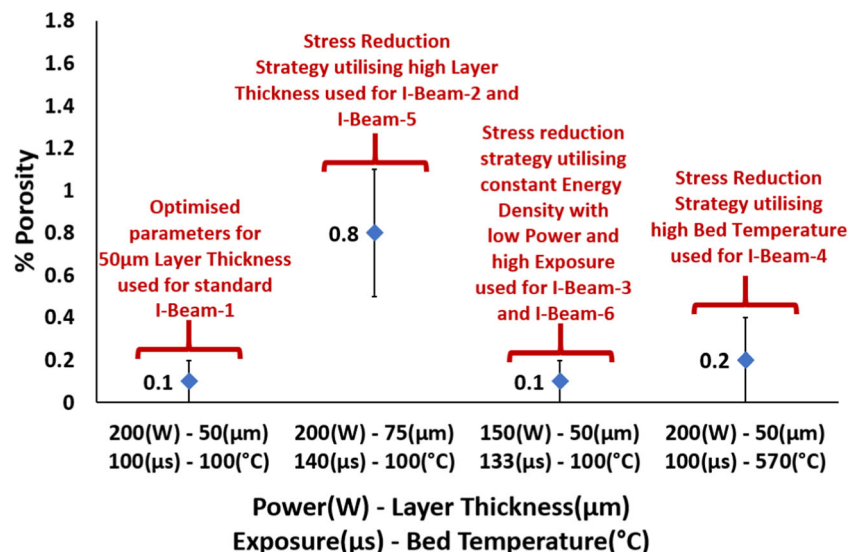
According to the results shown in Figs. 6b and 8, a more uniform stress distribution was measured in the region 4 of test case IB-2 compared with test case IB-1. From a component point of view, this can be considered as an improvement as stress hot spots can be detrimental for the preferential failure of parts. Stress hot spot is a higher stress concentration over a

small area, causing issues such as hot tearing. The observed reduction of the area corresponding to residual stress of 320 MPa in region 4 with the application of 75- $\mu\text{m}$  layer thickness could be due to the reduced cooling rate due to the application of a larger layer thickness [5, 8, 9, 34].

The results in Figs. 6c and 8 show that with the application of 150 W power and 133- $\mu\text{s}$  exposure to region 4 for test case IB-3 increased the % area of maximum residual stress (320 MPa) in region 4 for the cross-section of test case IB-3 to 51.1%. Test case IB-3 showed an increase of 101% in 320-MPa residual stress region compared to the standard I-Beam, test case IB-1. Figures 6c and 8 show that, for test case IB-3, 160-MPa residual stress region area reduced by 26.7% and the 80-MPa residual stress region area decreased by 79.7% compared with test case IB-1. Overall, the stress in region 4 (and summation of all stresses in regions 1–4) has increased. This is a surprising result considering findings from the work by Ali et al. [40] reporting the contrary.

The results in Figs. 6d and 8 show that building the I-Beam geometry at a bed pre-heat temperature of 570 °C, for test case IB-4, resulted in reduced overall residual stress in region 4 for the cross-section of test case IB-4. Test case IB-4 showed no 320-MPa residual stress region. Figures 6d and 8 show that,

**Fig. 3** Density analysis for optimised parameters used for standard I-Beam (test case IB-1) compared with parameters utilised for the stress reduction strategies



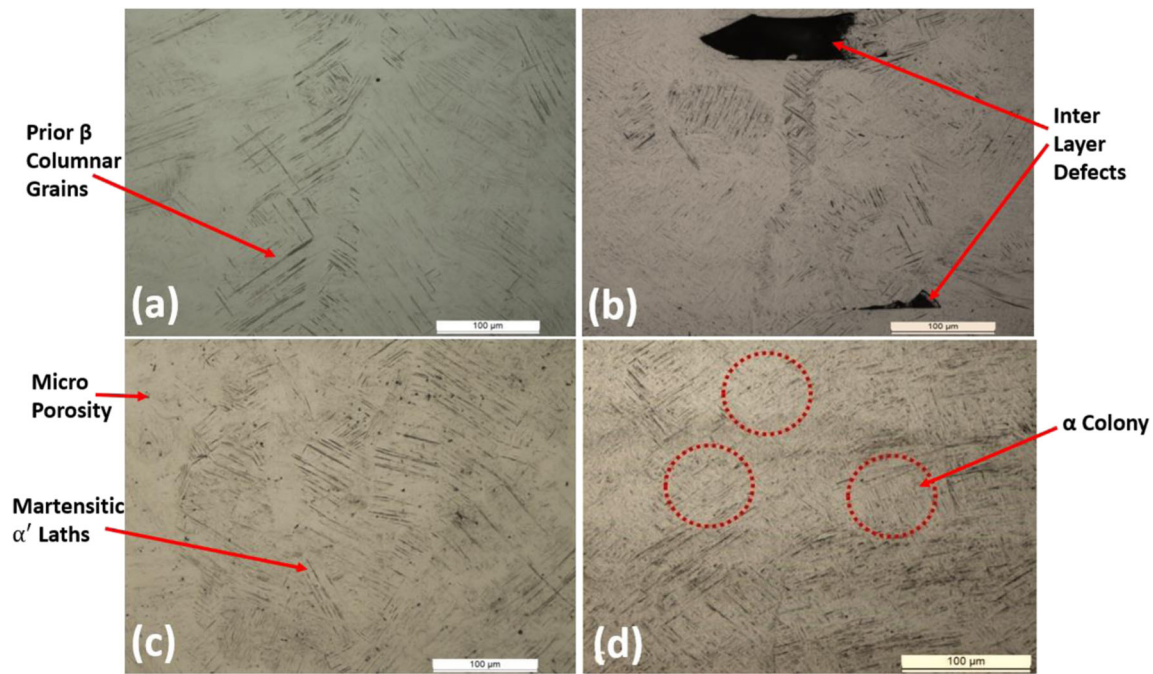


**Fig. 4** Microstructural analysis for optimised parameters used for standard I-Beam (test case 1) compared with parameters utilised for the stress reduction strategies. **a** Standard, 200 W, 100  $\mu$ s, 50  $\mu$ m and 100 °C;

**b** 200 W, 140  $\mu$ s, 75  $\mu$ m and 100 °C; **c** 150 W, 133  $\mu$ s, 50  $\mu$ m and 100 °C; **d** 200 W, 100  $\mu$ s, 50  $\mu$ m and 570 °C

for test case IB-4, 160-MPa residual stress region area reduced by 70.5%, while the 80-MPa residual stress region area increased by 34.9% compared with test case IB-1. Overall, it can be seen that region 4 of test case IB-4 presents a much lower stress distribution compared with test case IB-1. The beneficial effect of pre-heating the bed to a higher temperature on residual stress reduction has also been reported in references [11, 42, 64, 65]. Pre-heating the bed results in the reduction of thermal gradients and cooling rates, which in turn leads to the reduction of residual stress build up [42, 65]. It was reported in the work by Ali et al. [42]; bed pre-heat temperature of 570 °C totally eliminated the residual stress from block samples.

The small high-stress area (320 MPa) in region 4 of test case IB-4 can be attributed to the differential heat flow in the web and the supports of the upper flange. Part of the top flange

on the web will have higher heat flow to the substrate compared with the overhanging part. This would possibly lead to the central part of the top flange having a higher cooling rate compared with the overhanging region and thus as can be seen from Fig. 6d a higher stress distribution. The results from Figs. 6d and 8 show that pre-heating the bed is the best solution for the residual stress problem associated with SLM components.

The results in Figs. 6e and 8 show that with the application of 75- $\mu$ m layer thickness to region 3 (just below the identified high-stress region), for test case IB-5, reduced the percentage area of maximum residual stress (320 MPa) in region 4 for the cross-section of test case IB-5 to 23.1%. Test case IB-5 showed a reduction of 9.1% in 320-MPa residual stress region compared to the standard I-Beam, test case IB-1. Figures 6e and 8 show that, for test case IB-5, 160-MPa residual stress

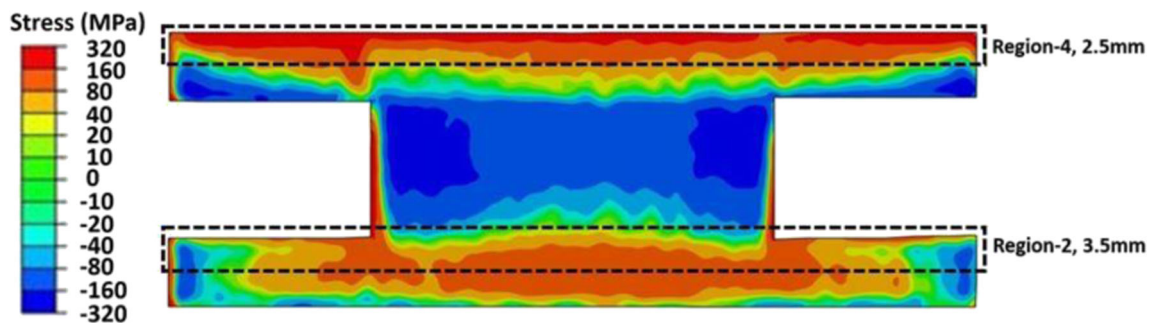


**Fig. 5** Residual stress (MPa) map in the I-Beam (test case IB-1) manufactured with standard parameters across all regions (high-stress regions indicated by dashed black lines, region 2 and region 4)



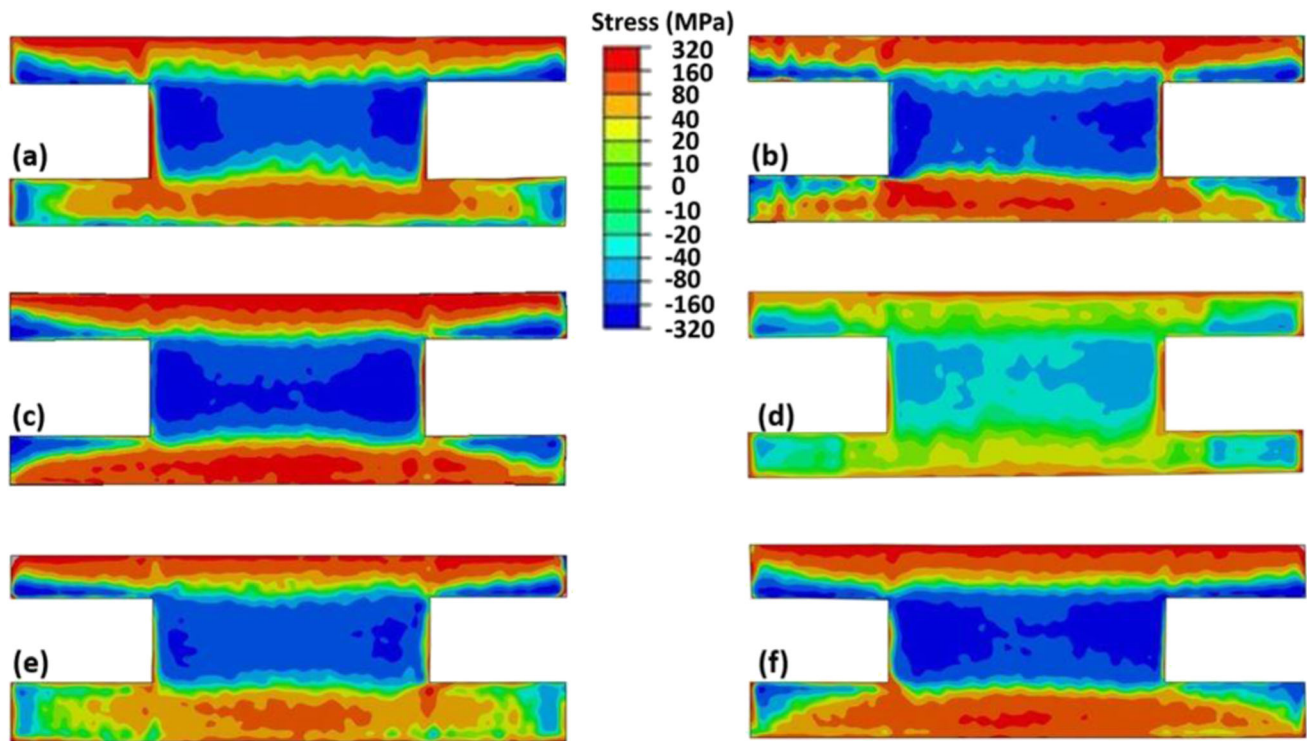


**Fig. 6** Comparison of residual stress (MPa), contour maps for various test cases **a** IB-1 (standard parameters), **b** IB-2 (75- $\mu\text{m}$  layer thickness for region 2 and region 4), **c** IB-3 (150 W power and 133- $\mu\text{s}$  exposure for region 2 and region 4), **d** IB-4 (570  $^{\circ}\text{C}$  bed pre-heating on Renishaw

SLM-125 machine), **e** IB-5 (75- $\mu\text{m}$  layer thickness for region 1 and region 3) and **f** IB-6 (150 W power and 133- $\mu\text{s}$  exposure for region 1 and region 3)

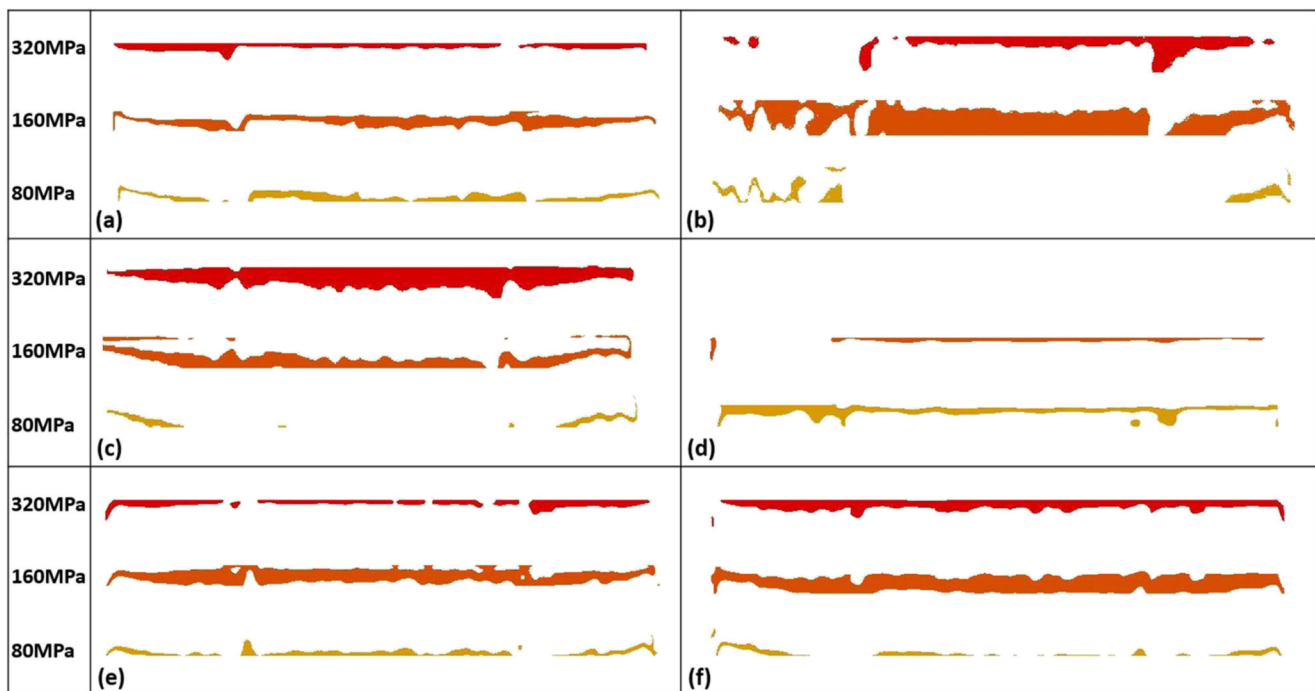


**Fig. 7** Region 4 areas corresponding to different stress levels for various test cases **a** IB-1 (standard parameters), **b** IB-2 (75- $\mu\text{m}$  layer thickness for region 2 and region 4), **c** IB-3 (150 W power and 133- $\mu\text{s}$  exposure for region 2 and region 4), **d** IB-4 (570  $^{\circ}\text{C}$  bed pre-heating on Renishaw

SLM-125 machine), **e** IB-5 (75- $\mu\text{m}$  layer thickness for region 1 and region 3) and **f** IB-6 (150 W power and 133- $\mu\text{s}$  exposure for region 1 and region 3)

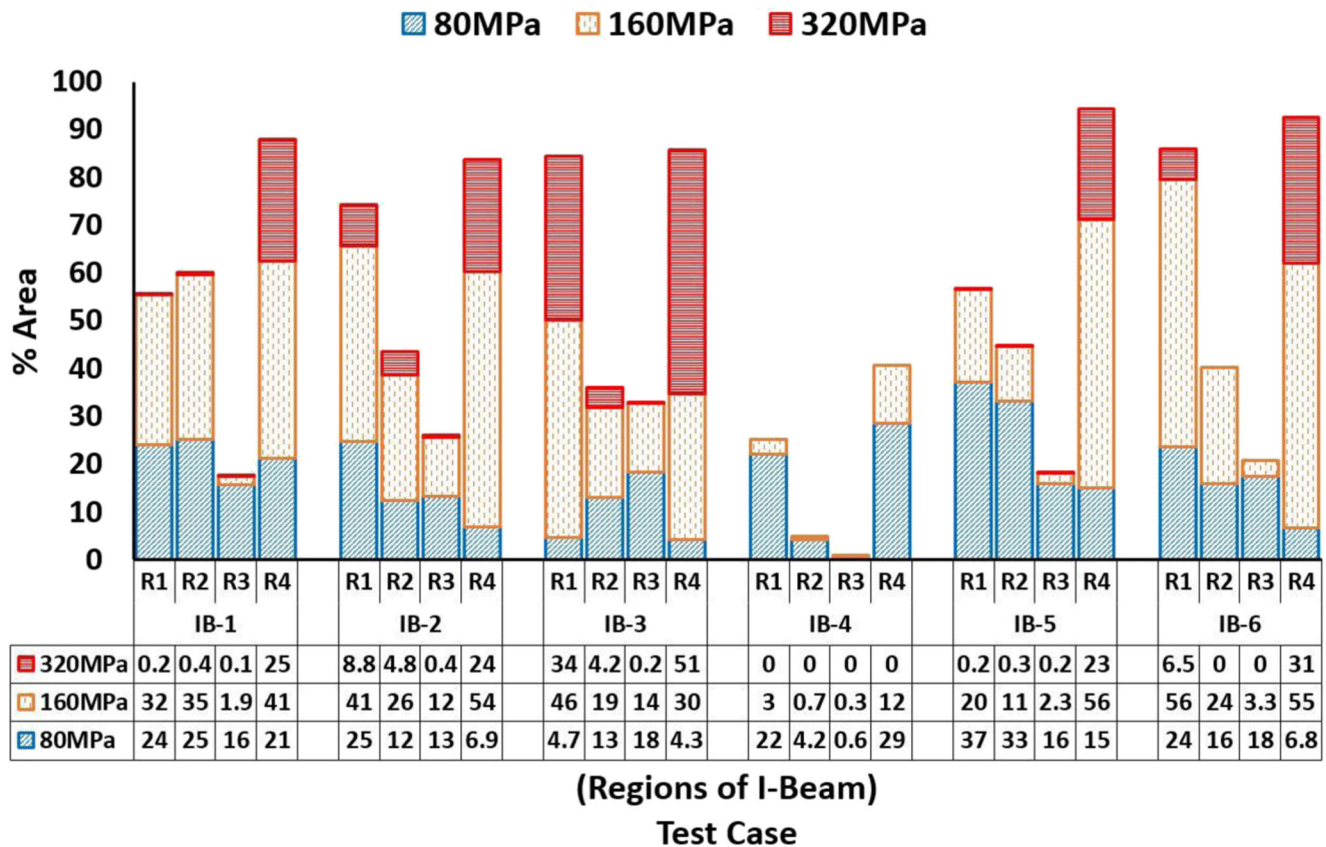


**Fig. 8** Residual stress variation in various test cases (table on X-axis shows % area of each region). **a** IB-1 (standard parameters), **b** IB-2 (75- $\mu$ m layer thickness for region 2 and region 4), **c** IB-3 (150 W power and 133- $\mu$ s exposure for region 2 and region 4), **d** IB-4 (570 °C

bed pre-heating on Renishaw SLM-125 machine), **e** IB-5 (75- $\mu$ m layer thickness for region 1 and region 3) and **f** IB-6 (150 W power and 133- $\mu$ s exposure for region 1 and region 3)

region area increased by 35.3% and the 80-MPa residual stress region area decreased by 28.3% compared with test case IB-1. Overall, it can be seen that region 4 of test case IB-5 presents a more uniform stress distribution compared with test case IB-1.

The results in Figs. 6f and 8 show that with the application of 150 W power and 133- $\mu$ s exposure to region 3 (just below the identified high-stress region 4), for test case IB-6, increased the percentage area of maximum residual stress (320 MPa) in region 4 for the cross-section of test case IB-6 to 30.5%. Test case IB-6 showed an increase of 20.1% in 320-MPa residual stress region compared to the standard I-Beam, test case IB-1. Figures 6f and 8 shows that, for test case IB-6, 160-MPa residual stress region area increased by 33.8% and the 80-MPa residual stress region area decreased by 67.9% compared with test case IB-1. Overall, it can be seen that region 4 of test case IB-6 presents a more uniform stress distribution compared with test case IB-1.

The results of Figs. 6 and 8 show that strategically applying stress reduction strategies to cross-sections of complex parts can lead to a reduction in residual stress. The application of stress reduction strategies to region 3 just below the high-stress region 4, for test cases IB-5 and IB-6, showed promising

results compared to test cases IB-2 and IB-3 where the stress reduction strategies were directly applied to region 4 (identified as a high-stress region in IB-1).

### 3.4.2 Effect of strategic stress reduction strategies on residual stress in high-stress Region 2

Figures 6 and 8 shows the variation of the measured residual stress in region 2 for the test cases using a strategic application of stress reduction parameters. The results in Figs. 6b and 8 show that with the application of 75- $\mu$ m layer thickness to region 2 (Identified as the high-stress regions see Fig. 5), for test case IB-2, increased the percentage area of maximum residual stress (320 MPa) in region 2 for the cross-section of test case IB-2 to 4.8%. Overall, it can be seen that region 2 of test case IB-2 presents a lower overall stress distribution compared with test case IB-1, except for a hot spot of 320 MPa generated just below the web. The application of 150 W power and 133- $\mu$ s exposure to region 2 (identified as the high-stress regions see Fig. 5), for test case IB-3, increased the percentage area of maximum residual stress (320 MPa) in region 2 for the cross-section of test case IB-3 to 4.2%. The

160-MPa residual stress region area reduced by 45.5% and the 80-MPa residual stress region area decreased by 48% compared with test case IB-1. Overall, it can be seen that region 2 of test case IB-3 presents a lower stress distribution compared with test case IB-1, except for a hot spot of 320 MPa, just below the web. As expected, the test case IB-4 resulted in a reduction in the overall residual stress in region 2 for the cross-section of the test case. Application of 75- $\mu$ m layer thickness to region 1 (just below the identified high-stress region 2), for test case IB-5, reduced the percentage area of maximum residual stress (320 MPa) in region 2 for the cross-section of test case IB-5 to 0.34%. Test case IB-5 showed a reduction of 15% in 320-MPa residual stress region compared to the standard I-Beam. The 160-MPa residual stress region area decreased by 67.2% and the 80-MPa residual stress region area increased by 32.1% compared with test case IB-1. Overall, it can be seen that region 2 of test case IB-5 presents a lower stress distribution compared with test case IB-1. Applying the stress reduction strategy to region 1, just below the high-stress region 2 resulted in a lower overall stress state for test case IB-5 compared with test case IB-2 when the same strategy was applied directly to the high-stress region 2. The application of 150 W power and 133- $\mu$ s exposure to region 3 (just below the identified high-stress region 2), for test case IB-6, eliminated the 320-MPa stress in region 2 for the cross-section of test case IB-6. Figures 6f and 8 show that, for test case IB-6, 160-MPa residual stress region area decreased by 29.6% and the 80-MPa residual stress region area decreased by 36.1% compared with test case IB-1. Overall, it can be seen that region 2 of test case IB-6 presents a lower stress distribution compared with test case IB-1.

The results of Figs 6 and 8 show that strategically applying stress reduction strategies to cross-sections of complex parts can lead to a reduction in residual stress. The application of stress reduction strategies to region 1 just below the high-stress region 2, for test cases IB-5 and IB-6, showed promising results compared to test cases IB-2 and IB-3 where the stress reduction strategies were directly applied to region 2 (identified as a high-stress region in IB-1).

### 3.4.3 Effect of strategic stress reduction strategies on residual stress in region 1

The application of 75- $\mu$ m layer thickness to region 2 increased the 320-MPa stressed region area in region 1 test case IB-2 by 4300% compared to the standard I-Beam, test case IB-1. The 160-MPa residual stress region area increased by 29.5% and the 80-MPa residual stress region area increased by 2.9% compared with test case IB-1. Overall, it can be seen that region 1 of test case IB-2 presents a higher stress distribution compared with test case IB-1. The application of 150 W power and 133- $\mu$ s exposure to region 2 for test case IB-3 increased the percentage area of maximum residual stress (320 MPa) in

region 1 by 17,000% in 320-MPa residual stress region compared to the standard I-Beam. The 160-MPa residual stress region area increased by 44.4% and the 80-MPa residual stress region area decreased by 80.5% compared with test case IB-1. Overall, it can be seen that region 1 of test case IB-3 presents a higher stress distribution compared with test case IB-1.

As expected with the application of 570 °C pre-heat for test case IB-4, it resulted in a reduction in the overall residual stress in region 1.

The application of 75- $\mu$ m layer thickness to region 1 did not affect the % area of maximum residual stress (320 MPa) in region 1 for the cross-section of test case IB-5. One hundred sixty-megapascal residual stress region area decreased by 37.8% and the 80-MPa residual stress region area increased by 53.9% compared with test case IB-1. Overall, it can be seen that region 1 of test case IB-5 presents a lower stress distribution compared with test case IB-1. Applying the stress reduction strategy to region 1, just below the high-stress region 2 resulted in a lower overall stress state for test case IB-5 compared with test case IB-2 when the same strategy was applied directly to the high-stress region 2.

The application of 150 W power and 133- $\mu$ s exposure to region 1 (just below the identified high-stress region 2), for test case IB-6, increased the 320 MPa stress area in region 1 for the cross-section of test case IB-6 by 3150% compared with test case IB-1. One hundred sixty-megapascal residual stress region area increased by 77.1% and the 80-MPa residual stress region area decreased by 1.7% compared with test case IB-1. Overall, it can be seen that region 1 of test case IB-6 presents a higher stress distribution compared with test case IB-1.

The application of stress reduction strategies to region 1, just below the high-stress region 2, for test cases IB-5 and IB-6, showed promising results compared to test cases IB-2 and IB-3 where the stress reduction strategies were directly applied to region 2 (identified as a high-stress region in IB-1). Even though Test case IB-6 showed an increase in the residual stress distribution in region 1.

### 3.4.4 Effect of strategic stress reduction strategies on residual stress in region 3

Overall, it can be seen that region 3 of test case IB-2 presents a slightly higher stress distribution compared with test case IB-1. Test case IB-3 presents a higher stress distribution compared with test case IB-1. Test case IB-4 presents a much lower stress distribution compared with test case IB-1. Test case IB-5 presents a slightly higher stress distribution compared with test case IB-1. Applying the stress reduction strategy to region 3, just below the high-stress region 4 resulted in a reduced overall stress state for test case IB-5 compared with test case IB-2 when the same strategy was applied directly to the high-stress region 4. Test case IB-6 presents a slightly



higher stress distribution compared with test case IB-1, even though the 320-MPa hot spots are eliminated. The application of stress reduction strategies to region 3 just below the high-stress region 4, for test cases IB-5 and IB-6, showed promising results compared to test cases IB-2 and IB-3 where the stress reduction strategies were directly applied to region 4 (identified as a high-stress region in IB-1).

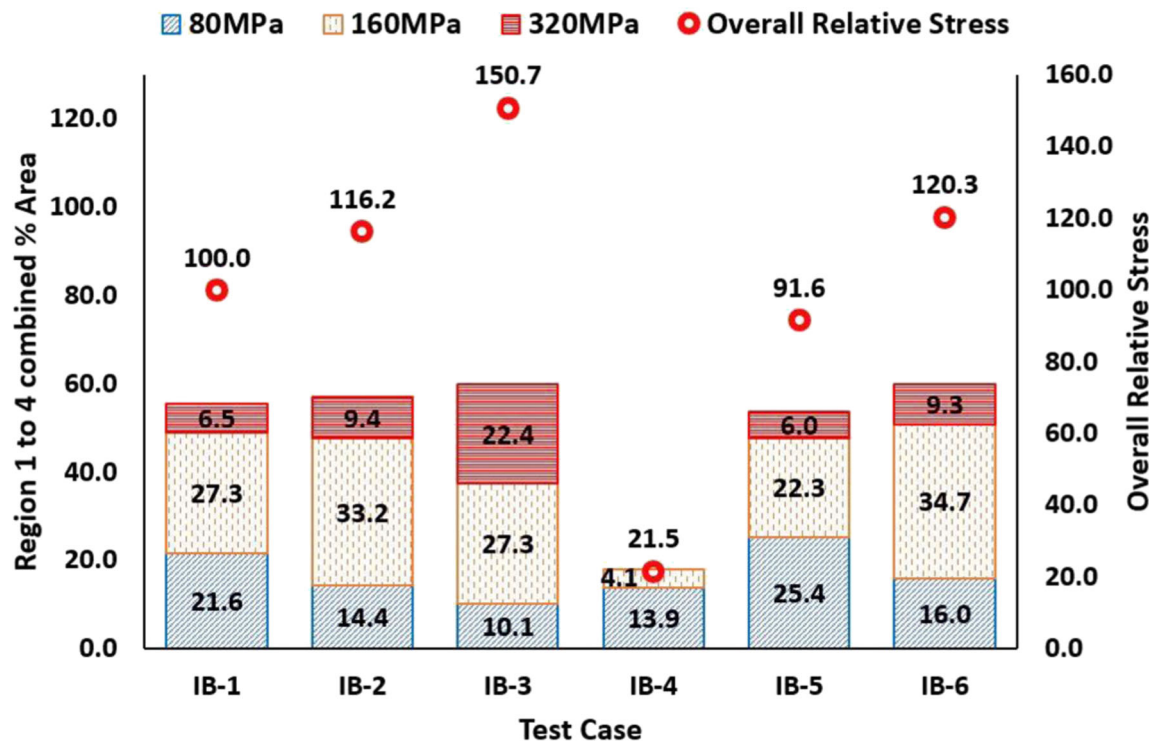
### 3.5 Overall effect of strategic stress reduction strategies on residual stress

Figure 9 shows the overall variation of residual stress for various test cases with strategic application of stress reduction parameters. The results in Fig. 9 show that overall pre-heating the bed is the most viable solution for residual stress reduction in SLM Ti6Al4V components. The application of 75- $\mu\text{m}$  layer thickness to region 1 and region 3 (just below the identified high-stress regions see Fig. 5), for test case IB-5, resulted in an overall reduction in the residual stress in the I-Beam geometry compared to standard processing conditions ( $\sim 8.5\%$  overall reduction when considering 80–320-MPa stresses only). Application of constant energy densities while reducing laser power and increasing exposure time was not effective in overall reducing stress (increased overall stress) contrary to findings in the work by Ali et al. [40] that tested simple block specimens.

Results from the strategic application of stress reduction strategies across different regions of the cross-section of an I-Beam geometry showed a redistribution of residual stress profile. It can be seen from the analysis in Sections 3.4.1, 3.4.2, 3.4.3 and 3.4.4 that strategic application of stress reduction strategies can be a viable solution for reducing stress in critical regions of a component.

## 4 Conclusions

Irrespective of the region of application, all the applied and theorised stress reduction strategies resulted in redistribution/alteration of the original residual stress profile across the component. Contrary to other works, the use of lower powers and increased exposure times (for comparable standard processing energy density) increased the overall stress within component compared to standard fixed SLM processing parameters (by 20–50% depending on regions applied for measured 80–320-MPa residual stress range). These earlier studies tested simple block specimens and hole drilling was used for stress analysis. Therefore, results may not be applicable to this study where a change in component cross-section is experienced. As expected, the application of a 570 °C in situ pre-heat resulted in an overall reduction in residual stress in the I-Beam sample across all regions.



**Fig. 9** Overall residual stress variation in various test cases. **a** IB-1 (standard parameters), **b** IB-2 (75- $\mu\text{m}$  layer thickness for region 2 and region 4), **c** IB-3 (150 W power and 133- $\mu\text{s}$  exposure for region 2 and

region 4), **d** IB-4 (570 °C bed pre-heating on Renishaw SLM-125 machine), **e** IB-5 (75- $\mu\text{m}$  layer thickness for region 1 and region 3) and **f** IB-6 (150 W power and 133- $\mu\text{s}$  exposure for region 1 and region 3)



Applying an increased 75- $\mu$ m layer thickness just below the identified high-stress regions resulted in a reduction in residual stress in the I-Beam geometry, with an overall stress reduction of 8.5% (for residual stresses within the range of 80–320 MPa). This reduction in overall stress by temporarily applying the stress reduction strategy below layers that are anticipated to be highly stressed presents a positive opportunity for this technology. Current SLM systems anticipate and adapt processing parameters for support structures and the outer surface of structures (skin, overhanging surfaces); however, the adaptation for anticipated geometry-related stresses is not fully exploited. Temporarily switching from standard build parameters to those that are known to assist in redistributing or reducing stresses from problematic/sensitive locations within a component (i.e. prone to warpage) would be a key step in developing a more intelligent process. An intelligent process will be more reactive and engaged with component fabrication. It will allow parameter adaption on the fly, anticipating residual stresses layers ahead and thus reduce build and in-service part failures.

**Acknowledgements** Contour measurements and analyses were conducted at the contour facility at the Open University in Milton Keynes. The authors would like to acknowledge the contribution of staff at the Open University staff including Peter Ledgard who conducted the contour cuts and Dr. Sanjooram Paddea for data analyses.

**Funding information** The author would like to thank TWI and the EPSRC Future Manufacturing Hub in Manufacture using Advanced Powder Processes (MAPP) (EP/P006566/1) for their support during this investigation.

**Open Access** This article is distributed under the terms of the Creative Commons Attribution 4.0 International License (<http://creativecommons.org/licenses/by/4.0/>), which permits unrestricted use, distribution, and reproduction in any medium, provided you give appropriate credit to the original author(s) and the source, provide a link to the Creative Commons license, and indicate if changes were made.

## References

1. Burns M (1993) Automated fabrication: improving productivity in manufacturing. Prentice Hall, -Englewood Cliffs
2. Gibson I, Rosen DW, Stucker B (2009) Additive manufacturing technologies: rapid prototyping to direct digital manufacturing. Springer, pp 1–14
3. Casavola C, Campanelli SL, Pappalettere C (2008) Experimental analysis of residual stresses in the Selective Laser Melting process. In: Proceedings of the XIth International Congress and Exposition. Orlando, Florida USA
4. Papadakis, L, A. Loizou, Risse J, Bremen S, Schrage J. A thermo-mechanical modeling reduction approach for calculating shape distortion in SLM manufacturing for aero engine components. In: VRAP Advanced Research in Virtual and Rapid Prototyping, Portugal
5. Kruth J-P, Deckers J, Yasa E, Wauthlé R (2012) Assessing and comparing influencing factors of residual stresses in selective laser melting using a novel analysis method. *Proc Inst Mech Eng B J Eng Manuf* 226(6):980–991
6. Kruth J-P, Yasa E, Deckers J, Thijs L, Van Humbeeck J (2010) Part and material properties in selective laser melting of metals. In: 16th International Symposium on Electromachining (ISEM XVI), Shanghai-China
7. Matsumoto M, Shiomi M, Osakada K, Abe F (2002) Finite element analysis of single layer forming on metallic powder bed in rapid prototyping by selective laser processing. *Int J Mach Tools Manuf* 42(1):61–67
8. Zaeh MF, Branner G (2010) Investigations on residual stresses and deformations in selective laser melting. *Prod Eng* 4(1)
9. Van Belle LV, Boyer G, Claude J (2013) Investigation of residual stresses induced during the selective laser melting process. *Key Eng Mater* 554-557:1828–1834
10. Tatsuaki Furumoto TU, Aziz MSA, Hosokawa A, Tanaka R (2010) Study on reduction of residual stress induced during rapid tooling process- influence of heating conditions on residual stress. *Key Eng Mater* 487(488):785–789
11. Roberts IA (2012) Investigation of residual stresses in the laser melting of metal powders in additive layer manufacturing. University of Wolverhampton, p 246
12. Joe Elambasseril SF, Bringezu M, Brandt M (2012) Influence of process parameters on selective laser melting of Ti 6Al-4V components. RMIT University School of Aerospace, Mechanical and Manufacturing Engineering (SAMME)
13. Das S, Wohler M, Beaman J, Bourell D (1998) Producing metal parts with selective laser sintering/hot isostatic pressing. *JOM* 50(12):17–20
14. Verhaeghe F, Craeghs T, Heulens J, Pandelaers L (2009) A pragmatic model for selective laser melting with evaporation. *Acta Mater* 57(20):6006–6012
15. Lu Y, Wu S, Gan Y, Huang T, Yang C, Junjie L, Lin J (2015) Study on the microstructure, mechanical property and residual stress of SLM Inconel-718 alloy manufactured by differing island scanning strategy. *Opt Laser Technol* 75:197–206
16. Dunbar AJ, Denlinger ER, Heigel J, Michaleris P, Guerrier P, Martukanitz R, Simpson TW (2016) Development of experimental method for in situ distortion and temperature measurements during the laser powder bed fusion additive manufacturing process. *Addit Manuf* 12(Part A):25–30
17. Nickel AH, Barnett DM, Prinz FB (2001) Thermal stresses and deposition patterns in layered manufacturing. *Mater Sci Eng A* 317(1–2):59–64
18. Gusarov AV, Pavlov M, Smurov I (2011) Residual stresses at laser surface remelting and additive manufacturing. *Phys Procedia* 12: 248–254
19. Cheng B, Shrestha S, Chou K (2016) Stress and deformation evaluations of scanning strategy effect in selective laser melting. *Addit Manuf* 12(Part B):240–251
20. Safdar S, Pinkerton AJ, Li L, Sheikh MA, Withers PJ (2013) An anisotropic enhanced thermal conductivity approach for modelling laser melt pools for Ni-base super alloys. *Appl Math Model* 37(3): 1187–1195
21. Vasinonta A, Beuth JL, Griffith M (2006) Process maps for predicting residual stress and melt pool size in the laser-based fabrication of thin-walled structures. *J Manuf Sci Eng* 129(1):101–109
22. Van Zyl I, Yadroitsev I, Yadroitsava I (2015) Residual stresses in direct metal laser sintered parts
23. Parry L, Ashcroft IA, Wildman RD (2016) Understanding the effect of laser scan strategy on residual stress in selective laser melting through thermo-mechanical simulation. *Addit Manuf* 12(Part A):1–15
24. Pohl H et al Thermal stresses in direct metal laser sintering. In: Proceedings of the 12th solid freeform fabrication symposium, Austin, TX, p 2001

25. Wu AS, Brown DW, Kumar M, Gallegos GF, King WE (2014) An experimental investigation into additive manufacturing-induced residual stresses in 316L stainless steel. *Metall Mater Trans A* 45(13): 6260–6270
26. Mercelis P, Kruth J-P (2006) Residual stresses in selective laser sintering and selective laser melting. *Rapid Prototyp J* 12(5):254–265
27. Shiomi M, Osakada K, Nakamura K, Yamashita T, Abe F (2004) Residual stress within metallic model made by selective laser melting process. *CIRP Ann Manuf Technol* 53(1):195–198
28. Yadroitsev I, Krakhmalev P, Yadroitsava I (2014) Selective laser melting of Ti6Al4V alloy for biomedical applications: temperature monitoring and microstructural evolution. *J Alloys Compd* 583:404–409
29. Manvatkar V, De A, DebRoy T (2015) Spatial variation of melt pool geometry, peak temperature and solidification parameters during laser assisted additive manufacturing process. *Mater Sci Technol* 31(8):924–930
30. Alimardani M, Toyserkani E, Huissoon JP, Paul CP (2009) On the delamination and crack formation in a thin wall fabricated using laser solid freeform fabrication process: an experimental–numerical investigation. *Opt Lasers Eng* 47(11):1160–1168
31. Brückner F, Lepski D, Beyer E (2007) Modeling the influence of process parameters and additional heat sources on residual stresses in laser cladding. *J Therm Spray Technol* 16(3):355–373
32. Taha MA et al (2012) On selective laser melting of ultra high carbon steel: effect of scan speed and post heat treatment Selektives Laserschmelzen von hoch kohlenstoffhaltigen Stählen: Einfluss der Abtastgeschwindigkeit und der Wärmenachbehandlung. *Mater Werkst* 43(11):913–923
33. Ilie A, Ali H, Mumtaz K (2017) In-built customised mechanical failure of 316L components fabricated using selective laser melting. *Technologies* 5(1):9
34. Ali H (2017) Evolution of Residual Stress in Ti6Al4V components fabricated using Selective Laser Melting. In: *Mechanical engineering*. The University of Sheffield
35. Suffiarov VS, Popovich AA, Borisov EV, Polozov IA, Masaylo DV, Orlov AV (2017) The effect of layer thickness at selective laser melting. *Procedia Eng* 174:126–134
36. Guan K et al (2013) Effects of processing parameters on tensile properties of selective laser melted 304 stainless steel. *Mater Des* 50:581–586
37. Delgado J, Ciurana J, Rodríguez CA (2012) Influence of process parameters on part quality and mechanical properties for DMLS and SLM with iron-based materials. *Int J Adv Manuf Technol* 60(5):601–610
38. Mugwagwa L et al (2016) A methodology to evaluate the influence of part geometry on residual stresses in selective laser melting
39. Ali H, Ghadbeigi H, Mumtaz K Effect of scanning strategies on residual stress and mechanical properties of selective laser melted Ti6Al4V. *Mater Sci Eng A*
40. Ali H, Ghadbeigi H, Mumtaz K (2018) Processing parameter effects on residual stress and mechanical properties of selective laser melted Ti6Al4V. *J Mater Eng Perform* 27(8):4059–4068
41. Ali H, Ghadbeigi H, Mumtaz K (2018) Residual stress development in selective laser-melted Ti6Al4V: a parametric thermal modelling approach. *Int J Adv Manuf Technol* 97(5):2621–2633
42. Ali H, Ma L, Ghadbeigi H, Mumtaz K (2017) In-situ residual stress reduction, martensitic decomposition and mechanical properties enhancement through high temperature powder bed pre-heating of selective laser melted Ti6Al4V. *Mater Sci Eng A* 695:211–220
43. Grant PV, Lord JD, Whitehead PS (2006) Good Practice Guide No. 53-Issue 2: The Measurement of Residual Stress by Incremental Hole Drilling Technique. The National Physical Laboratory, UK
44. Rossini NS et al (2012) Methods of measuring residual stresses in components. *Mater Des* 35(0):572–588
45. Withers PJB, Bhadeshia HKDH (2001) Residual stress. Part 1 – measurement techniques. *Mater Sci Technol* 17(4):355–365
46. Prime MB (2000) Cross-sectional mapping of residual stresses by measuring the surface contour after a cut. *J Eng Mater Technol* 123(2):162–168
47. Prime MB, DeWald AT (2013) *The Contour Method*. In: Schajer GS (ed) *Practical Residual Stress Measurement Methods*, pp 109–138
48. Hosseinzadeh F, Kowal J, Bouchard PJ (2014) Towards good practice guidelines for the contour method of residual stress measurement. *J Eng* 2014:453–468
49. DeWald AT, Rankin JE, Hill MR, Lee MJ, Chen HL (2004) Assessment of tensile residual stress mitigation in alloy 22 welds due to laser peening. *J Eng Mater Technol* 126:465–473
50. DeWald AT, Hill MR (2009) Eigenstrain-based model for prediction of laser peening residual stresses in arbitrary three-dimensional bodies, part 2: model verification. *J Strain Anal Eng Des* 44(1):13–27
51. Zhang Y, Ganguly S, Edwards L, Fitzpatrick ME (2004) Cross-sectional mapping of residual stresses in a VPPA weld using the contour method. *Acta Mater* 52(17):5225–5232
52. Ganguly S et al (2003) Validation of the contour method of residual stress measurement in a MIG 2024 weld by neutron and synchrotron X-ray diffraction AU - Zhang, Y. *J Neutron Res* 11(4):181–185
53. Hosseinzadeh F, Toparli MB, Bouchard PJ (2011) Slitting and contour method residual stress measurements in an edge welded beam. *J Press Vessel Technol* 134(1):011402–011402-6
54. Woo W, Choo H, Prime MB, Feng Z, Clausen B (2008) Microstructure, texture and residual stress in a friction-stir-processed AZ31B magnesium alloy. *Acta Mater* 56(8):1701–1711
55. Prime MB et al (2006) Residual stress measurements in a thick, dissimilar aluminum alloy friction stir weld. *Acta Mater* 54(15): 4013–4021
56. Rangaswamy P et al (2005) Residual stresses in LENS® components using neutron diffraction and contour method. *Mater Sci Eng A* 399(1):72–83
57. Vrancken B et al (2014) Residual stress via the contour method in compact tension specimens produced via selective laser melting. *Scr Mater* 87(Supplement C):29–32
58. Ahmed T, Rack HJ (1998) Phase transformations during cooling in  $\alpha+\beta$  titanium alloys. *Mater Sci Eng A* 243(1–2):206–211
59. Tan X et al (2016) Revealing martensitic transformation and  $\alpha/\beta$  interface evolution in electron beam melting three-dimensional-printed Ti-6Al-4V. *Sci Rep* 6:26039
60. Xu W, Sun S, Elambasseril J, Liu Q, Brandt M, Qian M (2015) Ti-6Al-4V additively manufactured by selective laser melting with superior mechanical properties. *JOM* 67(3):668–673
61. Welsch G, Boyer R, Collings EW (1993) *Materials properties handbook: titanium alloys*. ASM International
62. Furumoto T et al (2010) Study on reduction of residual stress induced during rapid tooling process: influence of heating conditions on residual stress. *Key Eng Mater* 447
63. van Belle L, Vansteenkiste G, Claude Boyer J (2012) Comparisons of numerical modelling of the selective laser melting. 504-506:1067–1072
64. Vora P, Mumtaz K, Todd I, Hopkinson N (2015) AlSi12 in-situ alloy formation and residual stress reduction using anchorless selective laser melting. *Addit Manuf* 7:12–19
65. Vrancken B et al. Influence of preheating and oxygen content on Selective Laser Melting of Ti6Al4V. In: *Proceedings of the 16th RAPDASA Conference*. RAPDASA, Annual International Conference on Rapid Product Development Association of South Africa 4–6 November 2015. Pretoria, South Africa